



Cite this: *Mater. Horiz.*, 2023, 10, 4438

Received 23rd May 2023,  
Accepted 18th July 2023

DOI: 10.1039/d3mh00775h

[rsc.li/materials-horizons](http://rsc.li/materials-horizons)

**Photonics neuromorphic computing shows great prospects due to the advantages of low latency, low power consumption and high bandwidth. Transistors with asymmetric electrode structures are receiving increasing attention due to their low power consumption, high optical response, and simple preparation technology. However, intelligent optical synapses constructed by asymmetric electrodes are still lacking systematic research and mechanism analysis. Herein, we present an asymmetric electrode structure of the light-stimulated synaptic transistor (As-LSST) with a bulk heterojunction as the semiconductor layer. The As-LSST exhibits superior electrical properties, photosensitivity and multiple biological synaptic functions, including excitatory postsynaptic currents, paired-pulse facilitation, and long-term memory. Benefiting from the asymmetric electrode configuration, the devices can operate under a very low drain voltage of  $1 \times 10^{-7}$  V, and achieve an ultra-low energy consumption of  $2.14 \times 10^{-18}$  J per light stimulus event. Subsequently, As-LSST implemented the optical logic function and associative learning. Utilizing As-LSST, an artificial neural network (ANN) with ultra-high recognition rate (over 97.5%) of handwritten numbers was constructed. This work presents an easily-accessible concept for future neuromorphic computing and intelligent electronic devices.**

## Introduction

With the start of the information explosion age, computers based on the conventional von Neumann digital system framework have gradually been unable to keep up with the growing data processing demands. Moreover, this classic architecture

# High-performance asymmetric electrode structured light-stimulated synaptic transistor for artificial neural networks†

Yixin Ran,‡<sup>a</sup> Wanlong Lu,‡<sup>a</sup> Xin Wang,‡<sup>a</sup> Zongze Qin,‡<sup>a</sup> Xinsu Qin,<sup>b</sup> Guanyu Lu,<sup>a</sup> Zhen Hu,<sup>a</sup> Yuanwei Zhu, <sup>a</sup> Laju Bu <sup>b</sup> and Guanghao Lu \*<sup>a</sup>

## New concepts

In this work, we have prepared an asymmetric electrode structured light-stimulated synaptic transistor (As-LSST) with the DPP-DTT:N2200 bulk heterojunction as a photoactive semiconductor layer. This asymmetric electrode architecture generates a built-in electric field that accelerates the separation of photogenerated carriers at the heterogeneous interface, resulting in As-LSST with superior electronic performance, photosensitivity, responsiveness and stability than conventional symmetric electrode devices. The photosensitivity of the As-LSST is even better than most of the organic photonic transistors reported in the literature. Furthermore, due to the excellent photosensitivity, the As-LSST can complete a single light pulse synapse event at a very low operating voltage ( $1 \times 10^{-7}$  V) with a power consumption of only  $2.14 \times 10^{-18}$  J, much lower than the energy required for a single synapse event previously reported in humans. The As-LSST also has excellent synaptic plasticity, allowing it to simulate signal processing and conditional learning experiments. Moreover, the superior photosensitivity and excellent synaptic plasticity of the As-LSST enabled it to achieve recognition rates of over 97% for handwritten digits by using successive identical light and electrical pulse stimuli.

has a bottleneck in the data flow, which makes it take longer and use more energy to process complex data.<sup>1–7</sup> Consequently, the development of intelligent electronic devices with a quicker response time, lower energy usage, and simpler structure has received increasing attention.<sup>8–12</sup> In the past few years, there have been many attempts to construct intelligent electrical devices that work in a similar way to the nervous systems of living things interacting with their surroundings.<sup>13–18</sup> For instance, artificial synaptic electronic devices have been developed to implement neural network computing.<sup>19–24</sup> However, electronic neuromorphic computing systems are limited in the speed of operation due to the bandwidth-connection density trade-off,<sup>25,26</sup> and further improvements in energy efficiency are difficult. Compared to electronics, photonics has shown promising applications in data processing. Synapses triggered by optical pulses are more suitable for ultra-high computational speeds because of their unique advantages, including high bandwidth, high interference immunity, and low-power

<sup>a</sup> Frontier Institute of Science and Technology, State Key Laboratory of Electrical Insulation and Power Equipment, Xi'an Jiaotong University, Xi'an, Shaanxi Province, 710054, China. E-mail: guanghao.lu@mail.xjtu.edu.cn

<sup>b</sup> School of Chemistry, Xi'an Jiaotong University, Xi'an, Shaanxi Province, 710049, China

† Electronic supplementary information (ESI) available. See DOI: <https://doi.org/10.1039/d3mh00775h>

‡ These authors contributed equally.

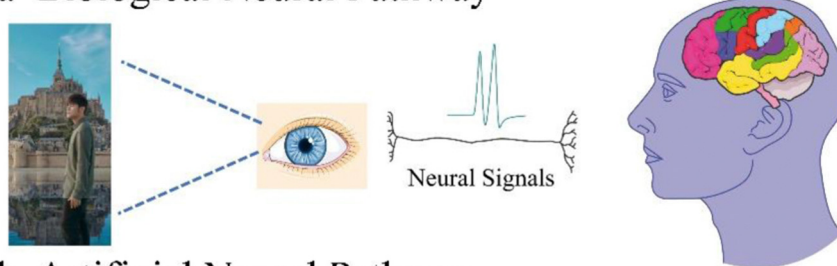
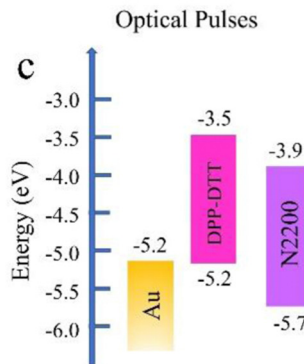
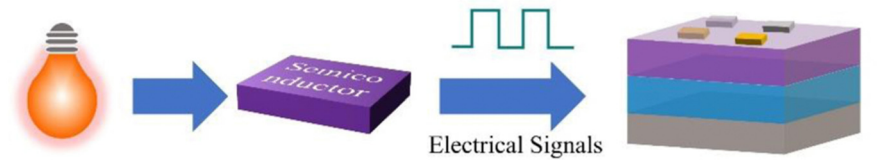
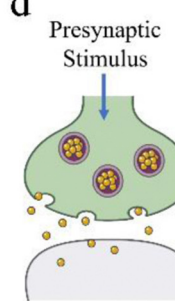
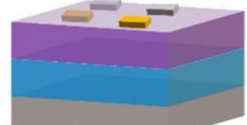
**a Biological Neural Pathway****b Artificial Neural Pathway**

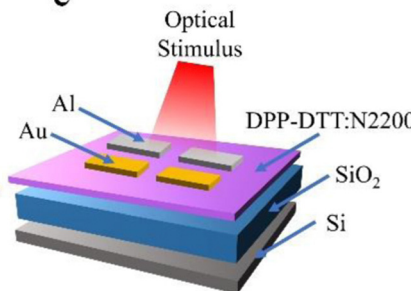
Photo-receptor



Electrical Signals



Synaptic Processing Unit

**e**

**Fig. 1** Symbolic representation of biological and artificial brain circuits. (a) Schematic diagram of the transmission of optical signals through neural networks in the human body. Optical information detected by the eye is transmitted through the visual network to the brain for processing. (b) Schematic representation of an optically mediated artificial neural network (ANN) in which photoreceptors perceive optical stimuli and synaptic processing units convert optical responses into electrical signals to produce neuromorphic responses. (c) The energy levels of materials used in photoreceptors. (d) Schematic diagram of a biological synapse. (e) An artificial synaptic device studied in this work.

computation.<sup>27–32</sup> More importantly, in higher animals, sensations detected by sensory organs (eyes, nose, ears, tongue, *etc.*) are relayed through complex neural networks to synaptic units in the brain for processing, generating different electrical impulse signals (Fig. 1a),<sup>33</sup> and 80% of the external environment information is acquired through the visual perception system.<sup>34–36</sup> Synaptic devices modulated by photonic signals facilitate the imitation of retinal neurons in the real eye, thus bridging the gap between the brain's computational and visual systems.

Nowadays, organic field effect transistors (OFETs) are considered as one of the most promising structures for the development of artificial synaptic devices. OFETs typically use symmetric electrodes and enable the transition from nonvolatile memories to artificial synaptic devices and photonic transistors by tuning the p-type/n-type semiconductor heterojunction structure.<sup>37,38</sup> However, photostimulated synaptic transistors based on symmetrical electrode OFETs have high energy consumption, limiting the application possibilities for building low-power artificial neural network systems.<sup>39,40</sup> Fortunately, OFETs with asymmetric electrodes generate a built-in electric field due to the difference in the source and drain work

functions, which enables the fast separation of photogenerated carriers at the heterogeneous interface, enhancing performance and improving the response speed and sensitivity.<sup>41–46</sup> On the other hand, the asymmetric electrode structure can greatly reduce the power consumption of transistor devices and facilitate organic electronic devices to improve the electrical and optical properties and enrich functionality.<sup>47–50</sup>

Therefore, herein, an artificial neural network (ANN) based on an asymmetric electrode structured light-stimulated synaptic transistor (As-LSST) was designed, which simulates the structure of the simplest monosynaptic neural network. Our system consists of two parts (Fig. 1b): a DPP-DTT:N2200 bulk heterojunction that acts as a photoreceptor and responds to light stimuli. A synaptic device with an asymmetric electrode structure acts as a processing unit to convert the light response into an electrical signal, mimicking synaptic behavior. By establishing synaptic neural networks, the ANN can achieve basic neural network functions such as learning and memory with low power consumption. In addition, optical logic functions ("AND" and "OR" operations), conditioning training, and handwritten digit recognition are also successfully implemented by ANN. On this basis, we also systematically investigate intelligent photosynapses

constructed from asymmetric electrodes and propose possible mechanisms of operation.

## Results and discussion

Organic semiconductors are widely used for applications in devices such as light emitting diodes, organic field-effect transistors and photovoltaics due to their properties of solution-processable, flexibility and light weight. Conjugated polymers represent a class of semiconductor materials which are usually used for the fabrication of high-performance organic devices. Heterojunctions composed of p-type and n-type organic semiconductors, poly[2,5-(2-octyldodecyl)-3,6-diketopyrrolopyrrole-*alt*-5,5-(2,5-di(thien-2-yl)thieno[3,2-*b*]thiophene)] (DPP-DTT) and poly[[1,2,3,6,7,8-hexahydro-2,7-bis(2-octyldodecyl)-1,3,6,8-dioxobenzo[IMn][3,8]phenanthroline-4,9-diyl][2,2'-bithiophene]-5,5'-diyl] (N2200) are excellent candidates for the fabrication of organic optoelectronic devices. DPP-DTT has high mobility and good environmental stability,<sup>51</sup> while N2200 has good solubility in common organic solvents, excellent air stability and excellent electron mobility.<sup>52</sup> Furthermore, these two materials can form typical type-II band alignment, which is beneficial for trapping and storing charges.<sup>53</sup> Therefore, we selected DPP-DTT and N2200 for the heterostructure. The molecular structures of DPP-DTT and N2200 are shown in Fig. S1 (ESI<sup>†</sup>). The energy level structures of the DPP-DTT,<sup>51</sup> N2200,<sup>52</sup> Au, and Al electrodes are depicted in Fig. 1c. DPP-DTT is co-mixed with N2200 as an active layer that responds to external light pulse stimulation. A schematic representation of a biosynapse linking two adjacent neurons is shown in Fig. 1d. Action potentials regulate the accumulation and emission of ions that allow neurotransmitters to be released from the presynaptic neurons into the synaptic gap. These neurotransmitters then bind to receptors on the postsynaptic membrane and generate postsynaptic currents. The excitatory postsynaptic current (EPSC) behavior is caused by the discharge of excitatory neurotransmitters. Changes in the strength of connections between presynaptic and postsynaptic neurons in response to external stimuli are defined as synaptic plasticity, which is crucial to brain memory and learning. Inspired by the biological synaptic structure, we prepared a DPP-DTT:N2200 heterojunction transistor with an asymmetric electrode (Au/Al) to imitate the biological synaptic function (Fig. 1e). The light stimulus applied to the synaptic device is considered a presynaptic input, and the injection of photogenerated carriers causes the device to generate EPSC currents.

The comparison of asymmetrical electrode transistor current on/off ratio and photosensitivity performance in different ratios of N2200 blended with DPP-DTT has been shown in Fig. 2a. The transfer curves of different ratios of N2200 blended with DPP-DTT before and after experiencing light illumination are shown in Fig. S2 (ESI<sup>†</sup>). As can be seen from Fig. 2a and Fig. S2 (ESI<sup>†</sup>), when a small amount of N2200 (5%) is blended with DPP-DTT, the current on/off ratio is almost unaffected and the photosensitivity is significantly improved. As the N2200 ratio

increases, a large number of N2200 form a continuous network structure that provides a path for the transfer of electrons and the device current on/off ratio decreases rapidly.<sup>43</sup> Therefore, in this paper, the weight ratio of DPP-DTT to N2200 in the semiconductor layer is always 95% : 5%. The UV-Vis absorption spectra of pure DPP-DTT films, pure N2200 films and DPP-DTT:N2200 (95% : 5%) blended films are shown in Fig. 2b. DPP-DTT film has a strong characteristic absorption peak around 700 and 800 nm, while the N2200 film exhibits a strong absorption around 400 nm in the visible spectrum.

The energy level diagram of Au/DPP-DTT/Al is shown in Fig. S3 (ESI<sup>†</sup>). When using gold as the source and aluminum as the drain, almost no energy level difference between the work function (WF) of gold and the highest occupied molecular orbital (HOMO) of DPP-DTT, it can be considered as an Ohmic contact between the semiconductor and the metal. Carriers can be easily injected from the metal layer into the semiconductor layer, resulting in an increase in the number of carriers in the semiconductor layer and an increase in the current in the device. However, when aluminum is used as the source and gold is used as the drain, having an energy level difference of 0.9 eV between the WF of aluminum and the HOMO of the DPP-DTT forms an injection barrier that prevents the injection of holes from the metal into the DPP-DTT; this barrier is also known as the Schottky barrier (Fig. S3a, ESI<sup>†</sup>).<sup>47–50</sup> Due to the presence of the injection barrier, it is difficult for the carriers to reach the semiconductor layer and the device current decreases rapidly. Then, the electrical performance of the DPP-DTT:N2200 asymmetric electrode transistor device also demonstrated that different electrodes can tune the contact between the metal and the semiconductor, thus changing the device performance. When using gold as the source and aluminum as the drain, the transfer curves (Fig. 2c) and output curves (Fig. 2d) are similar to those of a conventional symmetrical gold electrode transistor device (Fig. S4, ESI<sup>†</sup>), with a threshold voltage ( $V_{th}$ ) of 24 V and a device current on/off ratio ( $|I_{on}|/|I_{off}|$ ) as high as  $3.29 \times 10^6$ . At a source-drain voltage ( $V_{ds}$ ) of -60 V, the source-drain current ( $I_{ds}$ ) is as high as  $1.2 \times 10^{-4}$  A, and the current has not yet reached the saturation region. However, when aluminum is used as the source and gold is used as the drain, the carriers need to conquer a potential barrier of 0.9 eV to reach the semiconductor layer, resulting in a subsequent reduction of the on-state current ( $|I_{on}|$ ) and off-state current ( $|I_{off}|$ ) in the transfer curve (Fig. 2e), with  $|I_{on}|$  dropping more and the threshold voltage dropping to -4.8 V with a current on/off ratio of  $3.06 \times 10^4$ , greatly reducing the power consumption of the device. And in the output curve (Fig. 2f), the source drain current ( $I_{ds}$ ) decreases significantly for the same source drain voltage (-60 V), and the current quickly reaches the saturation region and finally stabilizes at  $1.6 \times 10^{-6}$  A. As shown in Fig. S3b and c (ESI<sup>†</sup>), the Kelvin probe force microscope (KPFM) measures the surface potential of thin films when Au and Al are used as source electrodes, respectively. KPFM could reflect the contact potential difference between the work function of the electrodes and semiconductor, that is  $V_{CPD} = (\Phi_{tip} - \Phi_{sample})/(-e)$ .  $V_{CPD}$  is the contact potential

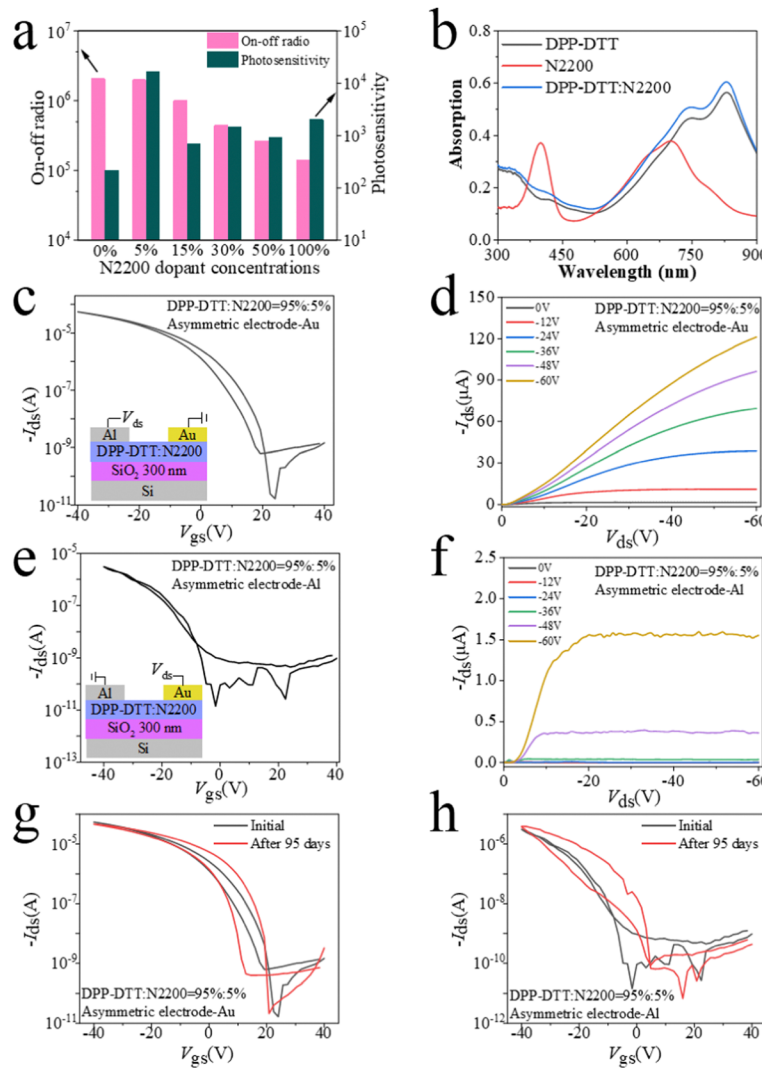


Fig. 2 (a) Comparison of on–off ratio and photosensitivity performance in different ratios of N2200 blended with DPP-DTT. (b) UV-Vis absorption spectra of the pure DPP-DTT film, the pure N2200 film, and the DPP-DTT:N2200 (95% : 5%) blend film. Electrical characteristics of the DPP-DTT:N2200 asymmetric electrode device. (c) and (e) Transfer curves, and the insets are corresponding device structure, employing gold (c) and aluminum (e) as source electrodes, respectively. (d) and (f) Output curves of the DPP-DTT:N2200 asymmetric electrode devices with gold (d) and aluminum (f) as source electrodes, respectively. Transfer curves of asymmetric electrode devices after 95 days in a glove box under a nitrogen atmosphere. (g) Gold was used as the source electrode. (h) Aluminum was used as the source electrode.

difference,  $\Phi_{\text{tip}}$  and  $\Phi_{\text{sample}}$  are the work function of the tip and sample, respectively, and  $e$  is the electronic charge. Therefore, the work function of Au is approximately 0.2 V higher than that of the semiconductor layer, which favors the transport of holes. In contrast, the work function of Al is smaller than that of the semiconductor layer by about 0.8 V. This greatly hinders the effective injection of holes. This result further confirms that Au is in ohmic contact with the semiconductor layer and Al is in Schottky contact with the semiconductor layer, which leads to different electrical properties. As shown in Fig. 2g, with gold as the source, the device can still reach a switching ratio of  $2.23 \times 10^6$  after 95 days stored in a glove box nitrogen atmosphere, which is close to the initial switching ratio of  $3.29 \times 10^6$ . With aluminum as the source (Fig. 2h), the threshold voltage of the device undergoes a rightward shift of 9.6 V after 95 days of

placement, and the switching ratio does not show a large decay. Therefore, the asymmetric electrode device in this work exhibits excellent stability.

The asymmetric electrode transistor and standard symmetric electrode transistor performance tests on photoresponse are shown in Fig. 3. The changes in the output curves of the devices with two different types of electrodes before and after experiencing light (intensity of  $4.45 \text{ mW cm}^{-2}$ ) are shown in Fig. 3a and c. Under the same test conditions ( $V_{\text{ds}} = -60 \text{ V}$ ), the output current of the asymmetric electrode transistor increases significantly, much more than that of the symmetric electrode transistor after light exposure. In order to obtain accurate light response data, the initial transmission curves of both transistors were measured in the dark. The transfer curves of the devices with two different types of electrodes at different light

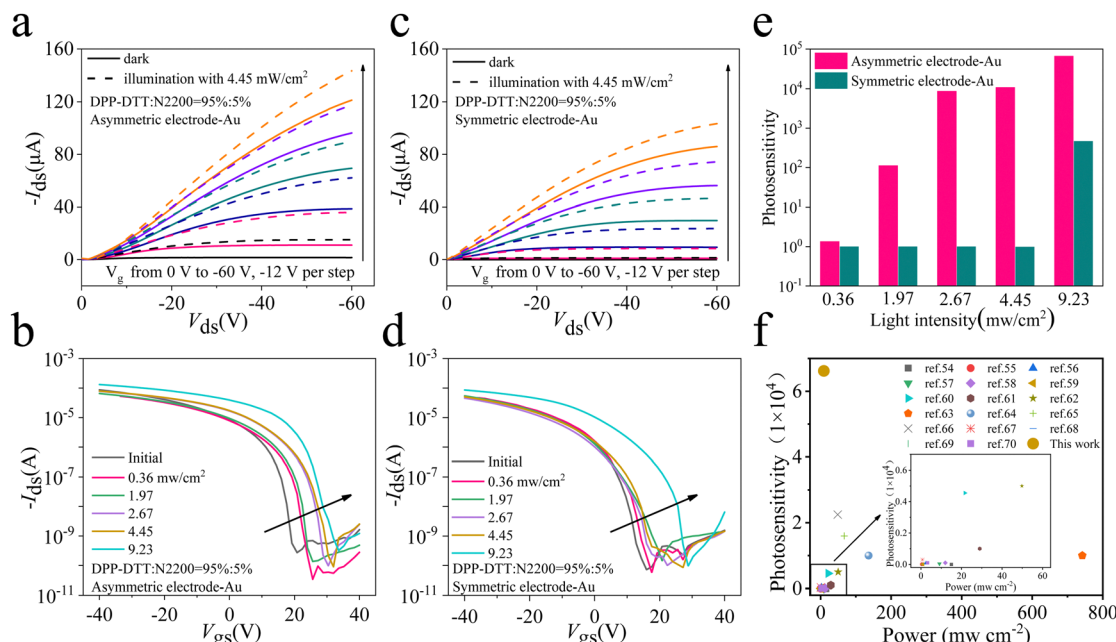


Fig. 3 (a) and (b) Photoresponse performance test of DPP-DTT:N2200 asymmetric electrode devices. (a) Output curves of the device in the dark and under illumination with  $4.45 \text{ mW cm}^{-2}$  light intensity. (b) Transfer curves of the device under different light intensities. (c) and (d) Photoresponse of DPP-DTT:N2200 symmetrical electrode devices. (c) Output curves of the device in the dark and under illumination with  $4.45 \text{ mW cm}^{-2}$  light intensity. (d) Transfer curves of the device under illumination with different light intensities. (e) Photosensitivity of the device under different light intensities. (f) Comparison of the photosensitivity of organic polymer photonic transistors for literature results and this work.

intensities are depicted in Fig. 3b and d. For the device with asymmetric electrodes, the threshold voltage in the initial transfer curve is about 20 V. Typically, when a positive gate bias or light is applied (defined as a “programming” process), the transfer curve shifts in a positive direction. It is clear that the threshold voltage rises dramatically with increasing incident light intensity, and even under weak light of  $0.36 \text{ mW cm}^{-2}$ , the threshold voltage can reach 25 V, demonstrating excellent photo-responsiveness. As a comparison, on the other hand, the threshold voltage of the symmetrical electrode device was controlled at around 19 V prior to light illumination, and the devices showed relatively weak light responses under all five different light intensities tested. The superior photosensitivity of asymmetrical electrode transistor devices can be clearly illustrated in Fig. 3b and d. Symmetrical electrode devices are less photosensitive than asymmetrical electrode devices, so the shift in the threshold voltage of the transfer curve to the right is not significant at low light intensities.

Photosensitivity ( $P$ ) is a key parameter to assess the superiority of photosensitive devices, and  $P$  can be defined by the following equation:  $P = |I_{\text{photo}}/I_{\text{dark}}|$ .  $I_{\text{dark}}$  and  $I_{\text{photo}}$  are the current of the transistor before and after illumination, respectively. The asymmetric electrode device exhibits excellent photosensitivity, showing  $P$  close to  $1 \times 10^4$  even at a low light intensity of  $2.67 \text{ mW cm}^{-2}$  (Fig. 3e). In contrast, the symmetrical electrode device has a lower photosensitivity, with  $P$  below  $5 \times 10^2$  even under intense light irradiation of  $9.23 \text{ mW cm}^{-2}$ . Thus, it is evident that the asymmetric electrode device has greater photosensitivity than the typical

symmetrical electrode device. Moreover, by comparing the photosensitivity of organic polymer photonic transistors reported in the literature (Fig. 3f),<sup>54-70</sup> the asymmetric electrode device in this work has superior photosensitivity and provides a novel design idea for next-generation photosensitive electronic devices. Increased photosensitivity of asymmetric devices is related to the energy level difference caused by the work function of different metal electrodes. After the semiconductor layer has been irradiated by light, photogenerated excitons are generated in the bulk heterojunction film. Photoelectrons are more easily transferred to N2200 due to the higher LUMO of DPP-DTT and photo-hole accumulation in DPP-DTT, and the heterostructure of DPP-DTT/N2200/DPP-DTT forms a potential barrier similar to a quantum well,<sup>37,38,71,72</sup> allowing some electrons in the channel to be trapped and stored in the N2200, as shown in Fig. S5a (ESI†). As a result, the concentration of electrons in the channel decreases and the threshold voltage of the device shifts in the positive direction. As shown in Fig. S5b (ESI†), the surface potential of the film increased after light irradiation. For two different metal electrodes, the difference in the work function will produce different Schottky barrier heights at the opposing metal contacts with successive built-in potentials. In our case, the work functions of Au and Al are 5.2 and 4.3 eV, respectively. Therefore, electrons will tend to flow from Al to Au, and a built-in potential can be generated along the direction of electron flow. Under illumination, photogenerated electrons flow to Al and holes flow to Au; as a result, a built-in potential is formed near both electrodes in the direction from the heterojunction to Au (and from Al to the heterojunction), which increases the built-in

potential of the whole active layer (Fig. S5b, ESI†). Subsequently, the accelerated transfer of free charge carriers to the corresponding metal electrodes increases the photosensitivity and speeds up the response.<sup>41–46</sup>

Therefore, a light-stimulated synaptic transistor with asymmetric electrodes (As-LSST) based on the DPP-DTT:N2200 heterojunction is fabricated. In these synaptic devices, the DPP-DTT:N2200 blends are used as a semiconductor layer to trap charge and also as a photoactive layer to simulate synaptic plasticity, and its conductivity is regarded as synaptic weight, which is expressed by EPSC to evaluate the performance of the synaptic device. Based on the UV-visible absorption spectroscopy of the DPP-DTT:N2200 films (Fig. 2b), we chose a 620 nm light pulse as the stimulation signal for the synaptic device.

Although the advantage of artificial neural networks in terms of energy consumption does not depend entirely on the performance of individual synaptic devices, optimizing the energy consumption of individual synaptic devices is still a key technology to achieve neuromorphic computing and sensing with efficient energy consumption.<sup>21,73</sup> The current variation of the DPP-DTT:N2200 As-LSST in response to a single light pulse at a wavelength of 620 nm ( $V_g = 0$  V,  $V_{ds} = 1 \times 10^{-7}$  V) is displayed in Fig. 4a. Under light stimulation of a specific wavelength, the current rises rapidly. When the light stimulation is removed, the current gradually decays slowly, which is similar to the EPSC behavior observed in biologically excitable synapses. In general, the energy consumption of an optoelectronic synaptic device can be determined using the following formulas:<sup>21</sup>

$$dE = P \times S \times dt \quad (1)$$

$$dE = V \times I \times dt \quad (2)$$

In eqn (1),  $P$ ,  $S$ , and  $dt$  represent the intensity of the light spike, the active region, and the duration of the light spike, respectively. This describes the energy consumption to generate the applied light spike. In eqn (2),  $V$ ,  $I$  and  $dt$  represent the reading voltage, postsynaptic current and duration of the light spike, respectively. It describes the energy consumption to generate the postsynaptic current at a light spike. Both methods are widely used to calculate the energy consumption of a photo-synaptic device. However, eqn (1) characterizes the photosensitivity of the device, while eqn (2) involves the electrical response to a light spike, which is more appropriate for characterizing the energy consumption of a photo-synaptic device.<sup>21,73,74</sup> We therefore use eqn (2) to characterize the power consumption of a single light pulse synaptic event. Due to the excellent photosensitivity of As-LSST, the energy consumption of the synaptic device is about  $2.14 \times 10^{-18}$  J when a light pulse of 100 ms duration is applied, which is close to the energy consumption per synaptic event in biological systems<sup>75</sup> (about 10 fJ). This provides a viable idea for designing low-power neuromorphic computing devices and also offers the possibility of optical synaptic devices that mimic the real eye and establish a connection between the brain's computational and visual systems.

Paired-pulse facilitation (PPF) is an important parameter to characterize short-term plasticity, which generates an important role in information recognition and analysis of biological systems, such as visual, olfactory, and auditory signals in the biological nervous system. Fig. 4b illustrates the PPF effect induced by the stimulation of two identical consecutive light

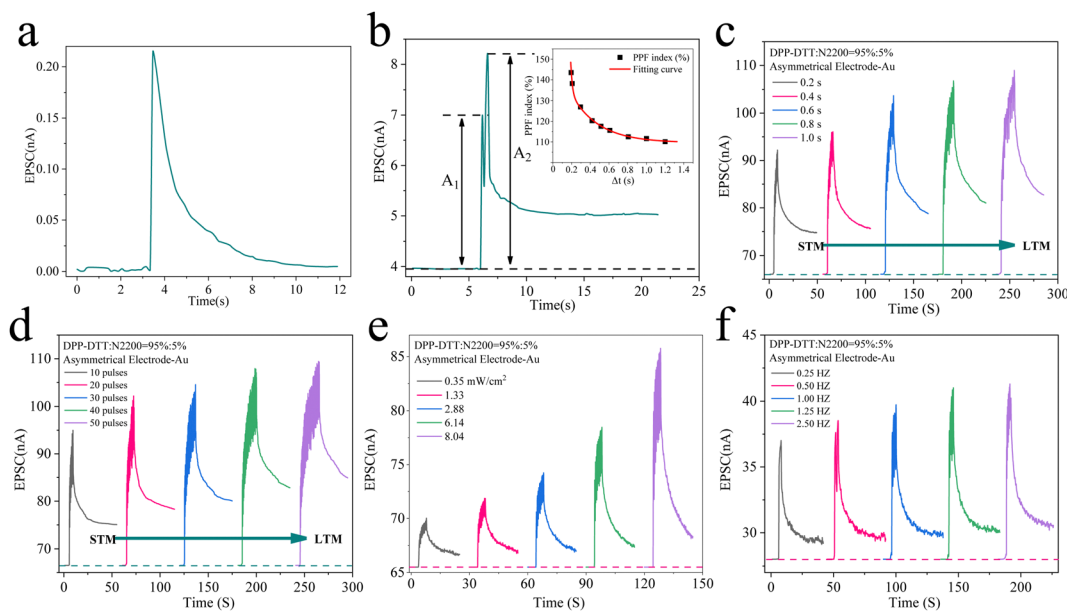


Fig. 4 (a) Excitatory postsynaptic currents (EPSCs) triggered by presynaptic light pulses ( $0.98 \text{ mW cm}^{-2}$ , 620 nm, 100 ms). (b) EPSCs triggered by a pair of light pulses ( $0.98 \text{ mW cm}^{-2}$ , 620 nm, 200 ms) with an interval of 200 ms. The transition from short-term memory (STM) to long-term memory (LTM) is triggered by increasing the (c) duration, (d) number, (e) light intensity, and (f) frequency of the light pulses. The measurement of (a) single synaptic behavior was performed at  $V_{ds} = -1 \times 10^{-7}$  V and  $V_g = 0$  V. The measurement of (b) synaptic behavior was performed at  $V_{ds} = -0.1$  V and  $V_g = 15$  V. The measurement of (c)–(f) synaptic behavior was performed at  $V_{ds} = -5$  V and  $V_g = 15$  V.

pulses with an interval time ( $\Delta t$ ) of 200 ms. Under the stimulation of light pulses, the photogenerated carriers generated by the film take some time to escape. Consequently, the EPSC triggered by the second light pulse is greater than the EPSC triggered by the first light pulse, indicating an excitation-promoted mechanism. The PPF index =  $A_2/A_1$  was introduced to further evaluate the synaptic properties of DPP-DTT:N2200 As-LSST, where  $A_2$  and  $A_1$  represent the current increase of EPSC triggered by the second and first light pulses, respectively, and the PPF index can reach 140% in our case ( $V_g = 15$  V,  $V_{ds} = -0.1$  V). In addition, we fit the dependence of the PPF index on  $\Delta t$  with a double exponential function.<sup>4,21,76</sup> PPF index =  $1 + C_1 \exp(-\Delta t/\tau_1) + C_2 \exp(-\Delta t/\tau_2)$ , where  $C_1$  and  $C_2$  represent the fast-phase and slow-phase facilitation amplitudes, respectively, while  $\Delta t$  represents the interval time. In our example,  $\tau_1 = 173$  ms and  $\tau_2 = 3000$  ms. This time scale is consistent with the range of time scales of biological synapses.<sup>4,21,76</sup>

The brain consolidates memory through learning, and memory levels can be categorized by retention time as short-term memory (STM) and long-term memory (LTM). In psychology, STM and LTM are regarded as the foundations of learning and memory, with the primary distinction being the longevity of memory. As depicted in Fig. S6 (ESI†), the brain encodes the acquired information and briefly stores it in the hippocampus, thereby producing STM. Subsequent learning and forgetting transform the STM into LTM. Typically, STM often lasts hundreds or thousands of milliseconds, whereas LTM refers to operations with longer durations. Since the level of memory depends on the duration, intensity, and frequency of learning, organisms usually achieve the transition from STM to LTM by rehearsing the training process. Therefore, to simulate synaptic plasticity further, an As-LSST device was designed that can be converted from STM to LTM by altering the duration, number, light intensity, and frequency of light pulses. The input light pulse stimulus is regarded as the training process, while the resulting EPSC is defined as the memory level. Complex processing

functions frequently require time sensitivity, as shown in Fig. 4c, where 10 consecutive light pulses are applied and when the duration of individual light pulses is increased from 0.2 s to 1.0 s, prolonged illumination induces enhanced EPSC and longer relaxation times compared to light pulses of shorter duration, and the memory retention time of As-LSST is significantly prolonged, exhibiting a dependence on the light pulse duration. It is clear that the EPSC rises gradually with increasing light pulse duration and exhibits a longer decay time, which is similar to the memory process in the human brain. The number of light pulses, light intensity and frequency exhibited comparable impacts on the learning and forgetting behavior of As-LSST (Fig. 4d, e and f). These results imply that the DPP-DTT:N2200 heterojunction As-LSST is capable of interconverting STM and LTM by virtue of its plasticity in terms of light pulse duration, number, light intensity and frequency. It is anticipated that As-LSST will be implemented in artificially intelligent sensory systems.

The EPSC decay of As-LSST after 50 light pulses training (light pulse wavelength: 620 nm, duration: 0.2 s, interval: 0.2 s) was recorded in Fig. 5a. As the number of stimuli increased from 10 to 50, the color of the two diagonal lines gradually became darker, indicating a dynamic learning process in the human brain. On the other hand, after removing the light pulses for 50 seconds, the color of the diagonal lines gradually faded and finally maintained at about 60% of the maximum learning current, showing good memory properties, which implies that DPP-DTT:N2200 As-LSST successfully mimicked the STM behavior.

Long-term memory formation in the brain involves three processes: learning, forgetting, and relearning. Human learning occurs in a stepwise manner, and the relearning process is more likely to recall the same information as the initial learning process. The DPP-DTT:N2200 heterojunction As-LSST can effectively simulate this step-by-step learning *via* repeated learning cycles. We simulated the learning function of the brain using

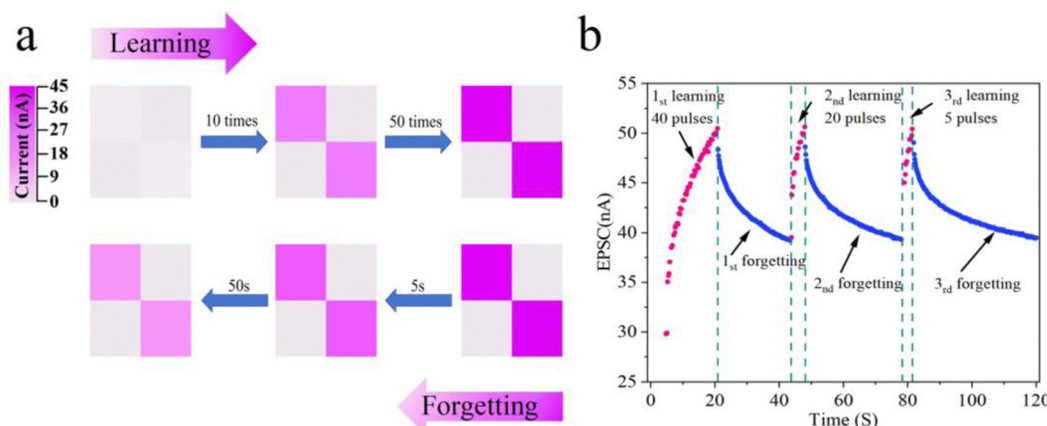


**Fig. 5** Learning, forgetting and relearning processes of the As-LSST processing unit. (a) Schematic diagram of As-LSST short-term memory (STM). The three images in the upper panel show the photocurrent changes excited by different numbers of light pulses; the three images in the lower panel show the photocurrent changes under different decay times. (Light pulse wavelength: 620 nm, duration: 0.2 s, interval time: 0.2 s). (b) Schematic diagram of As-LSST long-term memory (LTM). The learning, forgetting and relearning processes of LSST under 620 nm light pulse (duration: 0.2 s, interval: 0.2 s) are similar to those of the human brain.

three training sequences of light pulses (Fig. 5b). First, we applied 40 consecutive light pulses to stimulate the As-LSST in the first light pulse sequence, and the EPSC steadily rose as the number of pulses increased. Then, during a training interval of 23 s, the current dropped spontaneously to an intermediate level, comparable to the forgetting process of humans learning new information behavior. Thereafter, only 20 pulses were

needed in the second pulse sequence to reach the same level of learning as in the first training phase. Moreover, the time required for the current to decay to the same level becomes longer, taking 31 s, indicating an improvement in learning progress. Finally, only 5 successive light pulses are required to return to the previous storage level, with a longer memory time of 40 s. By repeating the learning-forgotten-relearning process,

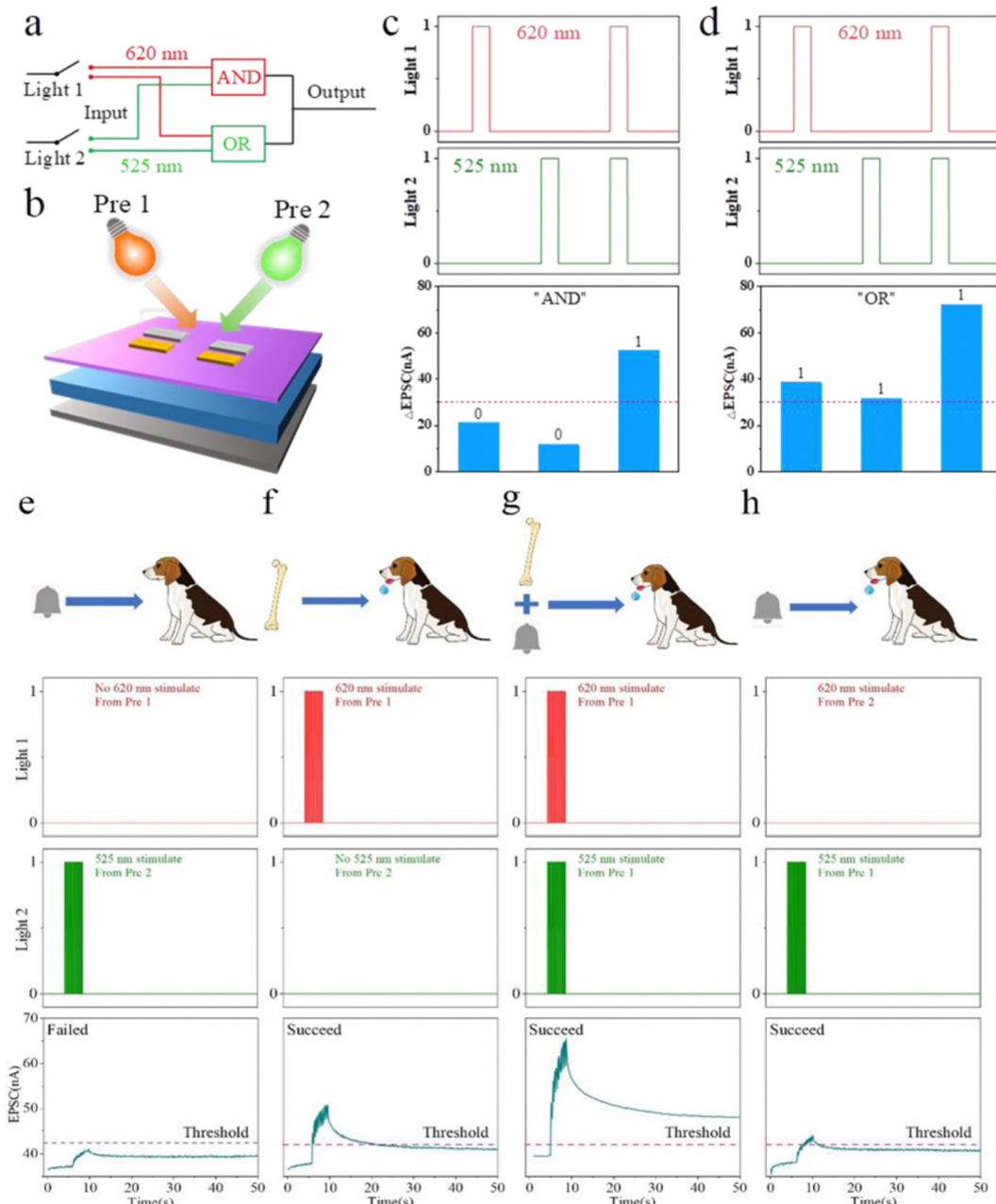


Fig. 6 (a) Schematic diagram of the optical logic function of the "AND" and "OR" operations. (b) Schematic diagram of device testing simulating Pavlov's learning. "AND" operation (c) and "OR" operation (d) for input (light 1 and light 2) characteristics and output (EPSC) characteristics. A training set contains a light pulse stimulus and the orange dashed line indicates that the logical function threshold was set to 30 mA. (e)–(h) Mimicking classical Pavlovian learning. One set of 620 nm light inputs and one set of 525 nm light pulses were used as food/unconditioned stimuli and ringing/conditioned stimuli, respectively (each training set contained ten light pulse stimuli). The duration and interval of each light pulse were 200 ms and 200 ms, respectively. The orange dashed line representing the salivary secretion threshold was set to 42 nA. Since the number of light pulses applied per group as well as the intensity in the logic function implementation and Pavlovian training are not the same, the thresholds set for the two experiments are different.

the As-LSST can be stimulated to achieve its learning goals, such as reaching a specified current value. It is noteworthy that the memory time gradually increases after each learning phase. This result is comparable to the fact that people forget some new information for a period of time but spend less time relearning to remember the forgotten information, and the more this process is repeated, the more pronounced the effect becomes, a phenomenon similar to the behavior of the human brain, indicating that the behavior of the brain for long-term memory has been successfully simulated. Importantly, this means that we can make the As-LSST with learning and relearning ability reach the learning goals autonomously by designing the period of learning stages rationally, such as the number, duration, and intensity of the impulses applied in the learning stages, which becomes the basis for achieving autonomous feedback in ANN.

Multiple signal inputs are frequently received by neurons in the nervous system, which then combine the information for interpretation through computational processing, such as logic functions. Therefore, the incorporation of logic functions into artificial synaptic devices is extremely valuable as it can significantly enhance their information processing capacities. As shown in Fig. 6a, light pulses of 525 nm and 620 nm of the same intensity and duration are used as input signals, while EPSC represents the output signal. A set training contains one light pulse. This demonstrates the optical logic function of the DPP-DTT:N2200 heterojunction As-LSST, including the “AND” and “OR” operations. Optically induced EPSC values greater than 30 nA are defined as logical “1” and values less than 30 nA are defined as logical “0”. Fig. 6b illustrates the DPP-DTT:N2200 heterojunction As-LSST logic function test diagram. The corresponding truth table grid is depicted in Fig. S7 (ESI†), including two optical inputs and two output values. Under “AND” operation, a 525 nm light pulse and a 620 nm light pulse ( $3.17 \text{ mW cm}^{-2}$ ) are applied simultaneously to the device and the EPSC value may exceed the threshold value (Fig. 6c). Under

the “OR” operation, when the light intensity was increased to  $9.12 \text{ mW cm}^{-2}$ , the induced EPSC values were greater than the threshold value when either or both of the 525 nm light pulses and 620 nm light pulses were applied simultaneously (Fig. 6d). Consequently, the experimental results imply that DPP-DTT:N2200 heterojunction As-LSST can perform controlled switching of the “AND” and “OR” logic functions by employing varied wavelengths and intensities of light, thereby permitting the simulation of neural computing.

DPP-DTT:N2200 heterojunction As-LSST was used to simulate Pavlov's classical conditioned reflex due to its synaptic plasticity with the number of light pulse stimuli. 525 nm wavelength light pulses were regarded as ringing/conditioned stimuli, whereas light pulses with a wavelength of 620 nm were termed food/unconditioned stimuli. EPSC induced by 10 successive light pulses at 525 nm and 620 nm respectively replicated conditioned and unconditioned responses. Since the number of light pulses applied per group as well as the intensity in the logic function implementation and Pavlovian training are not the same, the thresholds set for the two experiments are different; therefore, in Pavlov's classical conditioned reflex experiment, the EPSC = 42 nA was defined as the threshold of salivary response. Prior to training, bell stimulation alone resulted in a slight increase in EPSC below the threshold of the salivary response, whereas food stimulation significantly triggered the salivary response (Fig. 6e and f). During training, co-stimulation with food and a bell was employed to establish a connection between the bell and the salivary response (Fig. 6g). At the conclusion of training, the EPSC obtained by applying simply the bell stimulus was greater than the salivation threshold (Fig. 6h), showing that the dog had successfully learned to associate the bell with food. The successful simulation of Pavlovian associative learning marks the promising application of As-LSST in logic function and plasticity of conditioned reflexes.

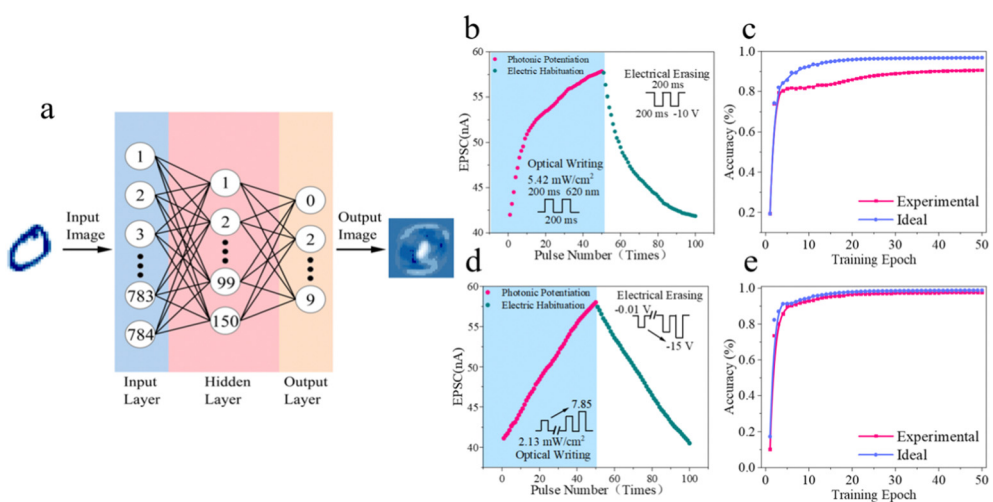


Fig. 7 Artificial neural network constructed by the As-LSST device for performing the pattern recognition task. (a) Schematic diagram of the artificial neural network used for the recognition task. As-LSST applies 50 consecutive identical light and electrical pulses, respectively. (b) Schematic diagram of EPSC variation. (c) Evolution of the recognition accuracy of handwritten digit “0”. As-LSST with 50 successive progressive light and electrical pulses applied, respectively. (d) Schematic diagram of EPSC variation. (e) Evolution of the recognition accuracy of the handwritten digit “0”.

Neural networks coupled by many neurosynapses in the human brain have sophisticated functions such as identifying images. Therefore, we use the constructed ANN to further demonstrate that the As-LSST device has the ability to learn and recognize. As shown in Fig. 7a, the ANN consists of 784 input neurons (corresponding to a  $28 \times 28$  pixel input image), 150 hidden neurons, and 10 output neurons (corresponding to the numbers 0–9), which are connected by synaptic weights. We applied 50 consecutive light pulses (620 nm,  $5.42 \text{ mW cm}^{-2}$ , duration: 0.2 s, interval: 0.2) and 50 consecutive electrical pulses ( $V_g = -10 \text{ V}$ , duration: 0.2 s, interval: 0.2 s) to the ANN (Fig. 7b), and the light pulses increased the electrical conductivity, which was partially offset by the electrical pulses, a phenomenon similar to a neurosynapse. We trained the ANN with 60 000 images from the Modified National Institute of Standards and Technology (MNIST) handwriting database, and then utilized 10 000 test images to calculate the recognition accuracy of 10 handwritten digits. As depicted in Fig. 7c, the overall recognition accuracy of the As-LSST-based ANN for handwritten digits undergoes a rapid growth phase at the outset and reaches a plateau as the training session lengthens. When the number of training sessions reaches 50, the overall recognition rate for digit 0 can reach 90%, and the recognition rate of the number 3 and the number 6 also reached more than 80% (Fig. S8, ESI<sup>†</sup>). Under the stimulation of light pulses, EPSC rises rapidly at the beginning, and the increase decreases gradually afterwards. Similarly, the EPSC decays gradually slower under the stimulation of negative voltage, causing a decrease in the linearity and symmetry of the EPSC curve and limiting the improvement of the handwritten digit recognition rate. To improve the linearity and symmetry of the EPSC curve, 50 consecutive unequal (increasing amplitude) light and electrical pulses were applied to the As-LSST (Fig. 7d). The light pulse intensity gradually increased from  $2.13 \text{ mW cm}^{-2}$  to  $7.85 \text{ mW cm}^{-2}$  and the EPSC increased smoothly. Similarly, the electrical pulse gradually increases from  $-0.01 \text{ V}$  to  $-15 \text{ V}$ , and the EPSC decays steadily. The linearity and symmetry of the EPSC curve are greatly improved, resulting in the improvement of the handwritten digit recognition rate (up to 97.5% for digit 0 after 50 training times, Fig. 7e).<sup>77–80</sup> The recognition rate for handwritten numbers 3 and 6 also exceeds 98%, demonstrating excellent recognition accuracy (Fig. S8, ESI<sup>†</sup>). This indicates that the ANN consisting of As-LSST has good prospects for applications in graphics recognition, memory computing and information sensing.

Fig. 8a shows the sub-layer absorption spectra resulting from the layer-by-layer phase subtraction method of FLAS. It is clear that the change in the aggregation structure along the longitudinal axis is directly related to the solvent evaporation process, and the absorption peaks of the sublayer are gradually redshifted along the depth axis, which implies a better molecular aggregation inside the film. As shown in Fig. S9 (ESI<sup>†</sup>), the difference in electrical performance was small for asymmetric devices with semiconductor layer concentrations of  $8 \text{ mg mL}^{-1}$  and  $10 \text{ mg mL}^{-1}$ , respectively. Therefore, the effect of concentration changes due to solvent

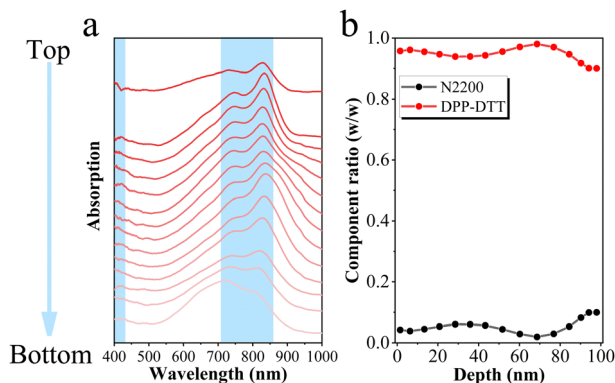


Fig. 8 DPP-DTT:N2200 blend film depth-dependent optical and electronic properties. (a) The film-depth-dependent light sublayer absorption spectra (FLAS). The blue line is a guide for the eye. (b) Composition map extracted from the FLAS spectrum.

volatilisation on the asymmetric electrode devices can be ignored. The thickness of the organic films was measured with an Asylum Research Cypher atomic force microscope (Fig. S10, ESI<sup>†</sup>). Based on the absorption spectra of the mixture of DPP-DTT and N2200 (Fig. 2b), the absorption peak at 800 nm was chosen as the characteristic peak of DPP-DTT and the absorption peak at 400 nm was chosen as the characteristic peak of N2200 to calculate the component distribution of DPP-DTT:N2200 films,<sup>81,82</sup> where the difference in peak position and intensity between the two absorption peaks was obvious, resulting in a smaller calculation error and more accurate calculation results. After that, we tested the surface roughness of the DPP-DTT:N2200 blend film by atomic force microscope (Fig. S11, ESI<sup>†</sup>), and it can be seen from the test result graph that the film has a good morphology with a roughness of only 1.38 nm.

A comparison of the performance and applications of bulk heterojunction organic field effect transistors is shown in Table 1. The results show that, due to the unique asymmetric electrode structure, the As-LSST simulates neurosynaptic behavior with a low doping rate of N-type semiconductors in the heterojunction, making a uniform distribution of components in the normal direction of the film and less prone to phase separation. As a result, the As-LSST in this work successfully simulates common neurosynaptic behavior, optical logic functions, and conditional learning without sacrificing the film quality, electrical performance, or photosensitivity. Thus, the As-LSST in this work successfully simulates common neurosynaptic behaviors, optical logic functions, and conditional learning without sacrificing the quality, electrical properties, and optical sensitivity of the film. Notably, in conjunction with Fig. 4–7 and Table 1, for a conventional heterojunction device with symmetric electrodes, the device behaves as a non-volatile memory without synaptic plasticity and conditional learning capability under the condition that only 5% of the n-type semiconductors are present. The implementation of digital recognition capability requires devices with synaptic plasticity and conditional learning capability. Therefore, the heterojunction

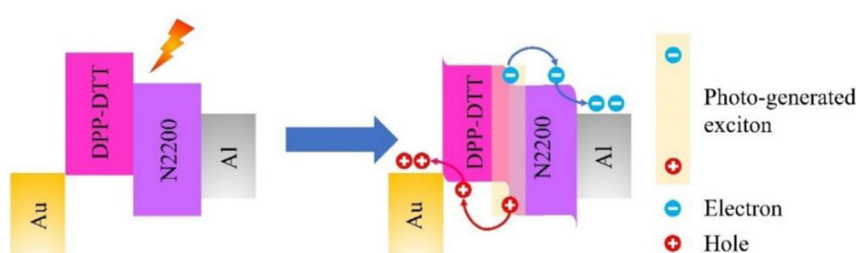
**Table 1** Comparison of the performance and applications of organic field effect transistor devices with P-type:N-type heterojunctions

Semiconductor	Device type	Electrode	Light source	$I_{\text{light}}/I_{\text{dark}}$	Ref.
PTCDA:AlClPc (50% AlClPc)	Phototransistor	Au/Au	405 nm 2.5 mW cm <sup>-2</sup>	<100	83
P3HT:THBT-ht (30% THBT-ht)	Phototransistor	Al/Al	808 nm 0.739 mW cm <sup>-2</sup>	$\approx 3 \times 10^2$	67
DPP-DTT:PC <sub>61</sub> BM (33% PC <sub>61</sub> BM)	Phototransistor	Au/Au	850 nm 1.886 mW cm <sup>-2</sup>	$\approx 80$	68
DPP-DTT:PC <sub>71</sub> BM (33% PC <sub>71</sub> BM)	Phototransistor	Au/Au	850 nm 1.886 mW cm <sup>-2</sup>	$\approx 100$	68
DPP-DTT:ITIC (33% ITIC)	Phototransistor	Au/Au	850 nm 1.886 mW cm <sup>-2</sup>	$\approx 10$	68
P3HT:EHD2FV (5% EHD2FV)	Phototransistor	Ag/Ag	700 nm 0.219 mW cm <sup>-2</sup>	$\approx 1.8$	69
PTB7:P(NDI2OD-T2) (50% P(NDI2OD-T2)	Phototransistor	Ag/Ag	675 nm 0.979 mW cm <sup>-2</sup>	<10	59
PTCDA:AlClPc:PbPc	Phototransistor	Au/Au	850 nm 29 mW cm <sup>-2</sup>	$10^3$	61
PDPP-DTT:PC <sub>61</sub> BM (67% PC <sub>61</sub> BM)	Phototransistor	Au/Au	808 nm 136 mW cm <sup>-2</sup>	$10^4$	64
DPP-DTT:PC <sub>61</sub> BM (50% PC <sub>61</sub> BM)	Phototransistor	Au/Au	808 nm 67 mW cm <sup>-2</sup>	$1.6 \times 10^4$	65
IDTB: N2200 (5% N2200)	Memory	Au/Au	675 nm 0.1 mW cm <sup>-2</sup>	$\approx 10$	84
PDVT-10:N2200 (3% N2200)	Memory	Au/Au	790 nm 5 mW cm <sup>-2</sup>	$\approx 100$	37
PDVT-10:N2200 (25% N2200)	Synapse	Au/Au	N/A	N/A	37
DPP:benzotriazole (40% benzotriazole)	Synapse	Au/Au	N/A	N/A	38
PDVT-10:PC <sub>61</sub> BM (15% PC <sub>61</sub> BM)	Synapse	Au/Au	N/A	N/A	85
IDTB:PC <sub>61</sub> BM (30% PC <sub>61</sub> BM)	Synapse	Au/Au	N/A	N/A	86
DPP-DTT:N2200 (5% N2200)	Phototransistor/Synapse	Au/Al	620 nm 9.23 mW cm <sup>-2</sup>	$6.62 \times 10^4$	This work

symmetric electrode device cannot achieve synaptic plasticity and therefore cannot achieve accurate recognition of handwritten digits. For the asymmetric electrode heterojunction device, the As-LSST is able to maintain excellent electrical and optical properties with the same heterojunction ratio (DPP-DTT:N2200 = 95%:5%), along with excellent synaptic plasticity and conditional learning ability due to the structural advantage of the asymmetric electrode. The linearity and symmetry of the LTP/LTD curve was then improved by gradually increasing the light intensity or decreasing the stimulation voltage, which resulted in accurate handwritten digit recognition (>97%) in As-LSST.

Fig. 9 demonstrates the method by which DPP-DTT:N2200 As-LSST generates photosynaptic phenomena under visible light with a positive gate voltage. When the semiconductor layer is irradiated by light, photogenerated excitons are generated in the hybrid film and holes move into the DPP-DTT and out through the gold electrode. The electrons then enter

the N2200 and exit via the aluminum electrode, completing the circuit. When the light irradiation stops, the photogenerated electrons decrease, and the generated current gradually decays, which is the reason for the appearance of the photosynaptic phenomenon. In comparison to the standard symmetrical gold electrode device (Fig. S12, ESI<sup>†</sup>), a Schottky contact is made between the gold electrode and N2200. As a result, electrons are constantly caught in N2200, and the device demonstrates a good memory effect at a DPP-DTT:N2200 ratio of 95%:5%. Then 10 light pulses (wavelength: 620 nm, duration: 0.2 s, interval: 0.2 s) are applied to the DPP-DTT:N2200 symmetrical gold electrode device, and after the light was withdrawn, the current of the device showed no substantial degradation and demonstrated excellent memory properties (Fig. S13, ESI<sup>†</sup>). The above results demonstrate the rationality of the working mechanism of As-LSST and strongly confirm that As-LSST devices can generate significant photosynaptic phenomena without sacrificing film quality, electrical properties or

**Fig. 9** Energy diagram of DPP-DTT:N2200 As-LSST during photosynaptic operation.

photoresponsiveness, thereby providing feasible ideas for the future development of high-performance light-stimulated synaptic transistors.

## Conclusions

In summary, the DPP-DTT:N2200 heterojunction asymmetric electrode light-stimulated synaptic transistor (As-LSST) has superior electrical properties and photoreactivity. The fundamental biological synaptic activities, including EPSC and PPF are mimicked upon As-LSST. Due to the excellent photosensitivity and the unique electrode structure of As-LSST, the power consumption can be as low as  $2.14 \times 10^{-18}$  J and the PPF index reaches 140%. In addition, the transition from STM to LTM was achieved by adjusting the light pulse stimulation conditions, including the light pulse duration, number, light intensity and frequency. More importantly, As-LSST achieved logic function and associative learning under light pulse stimulation. Afterwards, an artificial neural network (ANN) comprising As-LSST is demonstrated, which can be designed to complete the learning task by designing complex learning stages with different types of optical information, and the recognition accuracy of handwritten digits 0, 3 and 6 from the MNIST dataset reached more than 97.5% after 50 calendar hours. Consequently, unique As-LSST and ANN pave a promising path for the future realization of efficient neural network computing and intelligent artificial devices.

## Experimental

### Materials and devices

**Materials.** DPP-DTT and N2200 were purchased from Organotec Ltd without further purification.

**Device fabrication (Fig. S14, ESI†).** The bottom-gate top-contact organic field-effect transistor was fabricated on a Si/SiO<sub>2</sub> substrate, where n-type doped Si was used as the gate electrode, and 300 nm SiO<sub>2</sub> was used as the dielectric layer. The silicon wafers were cleaned with deionized water, acetone, and isopropyl alcohol in an ultrasonic bath for 10 min, and then blow-dried with N<sub>2</sub>. Next, the substrates were processed by O<sub>2</sub> plasma (FEMTO, 10 min). Then, the substrates were immersed in a toluene solution of OTS (OTS content of approximately 5%) for 120 minutes at 85 °C. DPP-DTT and N2200 were dissolved in chloroform at a concentration of 8 mg mL<sup>-1</sup>, respectively, and configured into a co-mingled solution according to the volume ratio DPP-DTT:N2200 = 95% : 5%, and then spin-coated on the substrate at 2000 rpm for 60 seconds. Subsequently, the organic semiconductor films are annealed at 200 °C for 30 min in a glove box. The customized shadow mask channel length was 300 μm and the channel width was 3 mm, and the customized shadow mask side was to ensure that only source or drain electrodes were deposited during the evaporation process. Finally, the gold film (50 nm) was deposited as the source electrode on the polymer film by thermal evaporation in a vacuum chamber (<6 × 10<sup>-4</sup> Pa) at a rate of 0.4–0.6 Å s<sup>-1</sup>.

Subsequently, about 50 nm of aluminum was deposited at a rate of 20 Å s<sup>-1</sup>.

### Thin film and OFET characteristics

OFET characteristics were measured by an Agilent Keysight B2900A Quick IV measurement system under ambient conditions (Fig. S15 and S16, ESI†). The source and drain voltages were controlled by setting CH1, and the gate voltage was set by adjusting CH2. The film morphology was characterized with an Asylum Research Cypher atomic force microscope in tapping mode. The variation of the film surface potential was obtained from the SPM-9700HT. The scaled size was 10 × 10 μm<sup>2</sup>. The absorbance of the films was measured by a Shimadzu UV-3600 spectrometer. The samples were prepared on glass substrates.

The digital identification experimental conditions were set up with an Agilent Keysight B2900A Quick IV measurement system. The experimental conditions are shown in Fig. S17 (ESI†). During the applied light pulse phase, the source drain voltage was kept at -5 V and the gate voltage was kept at 15 V, and the EPSC caused by the light pulse was gradually increased by setting the moving distance to keep the red light source close to the As-LSST to maintain the linearity of the curve. After applying the light pulse, a negative pulse is applied to the As-LSST, which gradually decreases from -0.01 V to -15 V after 50 pulses, thus ensuring the linear decay of the EPSC and the overall symmetry of the LTP/LTD curve.

The solar power meter (model LH-122) was used in this work to measure the light pulse intensity, which has a response spectral range of 400–1100 nm and a resolution of 1 μW cm<sup>-2</sup>.

### Author contributions

Yixin Ran: investigation, article analysis, writing original draft. Xin Wang: correction of the manuscript. Wanlong Lu: investigation, correction of the manuscript. Zongze Qin: article analysis. Xinsu Qin: investigation. Guanyu Lu: correction. Zhen Hu: correction. Yuanwei Zhu: editing. Laju Bu: editing. Guanghao Lu: editing, funding acquisition.

### Conflicts of interest

There are no conflicts to declare.

### Acknowledgements

This work is supported by the National Natural Science Foundation of China (Grant No. 52273026, 51873172, 21973072 and 51907148) and the Key Scientific and Technological Innovation Team Project of Shaanxi Province (2021GXZH-Z-055).

### References

- W. Wang, S. Gao, Y. Li, W. Yue, H. Kan, C. Zhang, Z. Lou, L. Wang and G. Shen, *Adv. Funct. Mater.*, 2021, **31**, 2101201.

2 Y. Zhang, Z. Wang, J. Zhu, Y. Yang, M. Rao, W. Song, Y. Zhuo, X. Zhang, M. Cui, L. Shen, R. Huang and J. Joshua Yang, *Appl. Phys. Rev.*, 2020, **7**, 11308.

3 Y. Li, J. Wang, Q. Yang and G. Shen, *Adv. Sci.*, 2022, **9**, 2202123.

4 X. Wang, Y. Ran, X. Li, X. Qin, W. Lu, Y. Zhu and G. Lu, *Mater. Horiz.*, 2023, DOI: [10.1039/D3MH00216K](https://doi.org/10.1039/D3MH00216K).

5 S. Dai, Y. Zhao, Y. Wang, J. Zhang, L. Fang, S. Jin, Y. Shao and J. Huang, *Adv. Funct. Mater.*, 2019, **29**, 1903700.

6 H. Han, H. Yu, H. Wei, J. Gong and W. Xu, *Small*, 2019, **15**, 1900695.

7 T. Guo, J. Ge, B. Sun, K. Pan, Z. Pan, L. Wei, Y. Yan, Y. N. Zhou and Y. A. Wu, *Adv. Electron. Mater.*, 2022, **8**, 2200449.

8 J. Shi, J. Jie, W. Deng, G. Luo, X. Fang, Y. Xiao, Y. Zhang, X. Zhang and X. Zhang, *Adv. Mater.*, 2022, **34**, 2200380.

9 S. Gao, G. Liu, H. Yang, C. Hu, Q. Chen, G. Gong, W. Xue, X. Yi, J. Shang and R. Li, *ACS Nano*, 2019, **13**, 2634.

10 H. Eslahi, T. J. Hamilton, S. Khandelwal and I. E. E. E. J. Explor, *Solid*, 2020, **6**, 122.

11 Z. Lv, Y. Zhou, S. Han and V. A. L. Roy, *Mater. Today*, 2018, **21**, 537.

12 S. Dai, Y. Wang, J. Zhang, Y. Zhao, F. Xiao, D. Liu, T. Wang and J. Huang, *ACS Appl. Mater. Interfaces*, 2018, **10**, 39983.

13 W. W. Lee, Y. J. Tan, H. Yao, S. Li, H. H. See, M. Hon, K. A. Ng, B. Xiong, J. S. Ho and B. C. K. Tee, *Science Robotics*, 2019, **4**, e219832.

14 Y. Shen, N. C. Harris, S. Skirlo, M. Prabhu, T. Baehr-Jones, M. Hochberg, X. Sun, S. Zhao, H. Larochelle, D. Englund and M. Soljacic, *Nat. Photonics*, 2017, **11**, 441.

15 A. Petritz, E. Karner-Petritz, T. Uemura, P. Schaffner, T. Araki, B. Stadlober and T. Sekitani, *Nat. Commun.*, 2021, **12**, 2399.

16 H. Jinno, T. Yokota, M. Koizumi, W. Yukita, M. Saito, I. Osaka, K. Fukuda and T. Someya, *Nat. Commun.*, 2021, **12**, 2234.

17 P. M. Sheridan, F. Cai, C. Du, W. Ma, Z. Zhang and W. D. Lu, *Nat. Nanotechnol.*, 2017, **12**, 784.

18 T. W. Hughes, M. Minkov, Y. Shi and S. Fan, *Optica*, 2018, **5**, 864.

19 Y. Zhao, C. Su, G. Shen, Z. Xie, W. Xiao, Y. Fu, S. Inal, Q. Wang, Y. Wang, W. Yue, I. McCulloch and D. He, *Adv. Funct. Mater.*, 2022, **32**, 2205744.

20 C. Han, X. Han, J. Han, M. He, S. Peng, C. Zhang, X. Liu, J. Gou and J. Wang, *Adv. Funct. Mater.*, 2022, **32**, 10586.

21 Y. Sun, M. Li, Y. Ding, H. Wang, H. Wang, Z. Chen and D. Xie, *InfoMat*, 2022, **4**, e12317.

22 J. Li, C. Ge, J. Du, C. Wang, G. Yang and K. Jin, *Adv. Mater.*, 2020, **32**, 1905764.

23 L. Yang, M. Singh, S. Shen, K. Chih, S. Liu, C. I. Wu, C. Chu and H. Lin, *Adv. Funct. Mater.*, 2020, **31**, 2008259.

24 Y. Zhu, N. Qiao, S. Dong, G. Qu, Y. Chen, W. Lu, Z. Qin, D. Li, K. Wu, Y. Nie, B. Liu, S. Li and G. Lu, *Chem. Mater.*, 2022, **34**, 6505.

25 S. Xiang, Y. Han, Z. Song, X. Guo, Y. Zhang, Z. Ren, S. Wang, Y. Ma, W. Zou, B. Ma, S. Xu, J. Dong, H. Zhou, Q. Ren, T. Deng, Y. Liu, G. Han and Y. Hao, *J. Semicond.*, 2021, **42**, 023105.

26 J. Zhang, S. Dai, Y. Zhao, J. Zhang and J. Huang, *Adv. Intell. Syst. ger.*, 2020, **2**, 1900136.

27 S. Dai, Y. Zhao, Y. Wang, J. Zhang, L. Fang, S. Jin, Y. Shao and J. Huang, *Adv. Funct. Mater.*, 2019, **29**, 1903700.

28 N. Ilyas, J. Wang, C. Li, D. Li, H. Fu, D. Gu, X. Jiang, F. Liu, Y. Jiang and W. Li, *Adv. Funct. Mater.*, 2022, **32**, 2110976.

29 J. Shen, Z. Cheng and P. Zhou, *Nanotechnology*, 2022, **33**, 372001.

30 H. Han, H. Yu, H. Wei, J. Gong and W. Xu, *Small*, 2019, **15**, 1900695.

31 Q. Zhang, T. Jin, X. Ye, D. Geng, W. Chen and W. Hu, *Adv. Funct. Mater.*, 2021, **31**, 2106151.

32 S. Song, J. Kim, S. M. Kwon, J. Jo, S. K. Park and Y. Kim, *Adv. Intell. Syst. ger.*, 2021, **3**, 2000119.

33 C. Han, X. Han, J. Han, M. He, S. Peng, C. Zhang, X. Liu, J. Gou and J. Wang, *Adv. Funct. Mater.*, 2022, **32**, 2113053.

34 K. He, Y. Liu, J. Yu, X. Guo, M. Wang, L. Zhang, C. Wan, T. Wang, C. Zhou and X. Chen, *ACS Nano*, 2022, **16**, 9691.

35 X. Han, Z. Xu, W. Wu, X. Liu, P. Yan and C. Pan, *Small Structures*, 2020, **1**, 2000029.

36 Y. Pei, Z. Li, B. Li, Y. Zhao, H. He, L. Yan, X. Li, J. Wang, Z. Zhao, Y. Sun, Z. Zhou, J. Zhao, R. Guo, J. Chen and X. Yan, *Adv. Funct. Mater.*, 2022, **32**, 2203454.

37 C. Gao, H. Yang, E. Li, Y. Yan, L. He, H. Chen, Z. Lin and T. Guo, *ACS Photonics*, 2021, **8**, 3094.

38 Y. Yang, Y. Wu, W. He, H. Tien, W. Yang, T. Michinobu, W. Chen, W. Lee and C. Chueh, *Adv. Sci.*, 2022, **9**, 2203025.

39 B. Yang, Y. Wang, Z. Hua, J. Zhang, L. Li, D. Hao, P. Guo, L. Xiong and J. Huang, *Chem. Commun.*, 2021, **57**, 8300.

40 T. Chen, X. Wang, D. Hao, S. Dai, Q. Ou, J. Zhang and J. Huang, *Adv. Opt. Mater.*, 2021, **9**, 2002030.

41 D. Hao, D. Liu, S. Zhang, L. Li, B. Yang and J. Huang, *Adv. Opt. Mater.*, 2022, **10**, 2100786.

42 C. Perumal Veeramalai, S. Yang, R. Zhi, M. Sulaman, M. I. Saleem, Y. Cui, Y. Tang, Y. Jiang, L. Tang and B. Zou, *Adv. Opt. Mater.*, 2020, **8**, 2000215.

43 J. Ding, H. Fang, Z. Lian, J. Li, Q. Lv, L. Wang, J. Sun and Q. Yan, *CrystEngComm*, 2016, **18**, 4405.

44 J. Lu, Z. Zheng, J. Yao, W. Gao, Y. Xiao, M. Zhang and J. Li, *Nanoscale*, 2020, **12**, 7196.

45 D. Han, K. Liu, Q. Hou, X. Chen, J. Yang, B. Li, Z. Zhang, L. Liu and D. Shen, *Sens. Actuators, A*, 2020, **315**, 112354.

46 K. Gu, Z. Zhang, H. Haofei, K. Tang, J. Huang, M. Liao and L. Wang, *J. Mater. Chem. C*, 2023, **11**, 5371–5377.

47 C. Yang, J. Qian, S. Jiang, H. Wang, Q. Wang, Q. Wan, P. K. L. Chan, Y. Shi and Y. Li, *Adv. Opt. Mater.*, 2020, **8**, 2000153.

48 Y. Kim, E. K. Lee and J. H. Oh, *Adv. Funct. Mater.*, 2019, 1900650.

49 D. Li, M. Zhao, K. Liang, H. Ren, Q. Wu, H. Wang and B. Zhu, *Nanoscale*, 2020, **12**, 21610.

50 J. M. Shannon, R. A. Sporea, S. Georgakopoulos, M. Shkunov and S. R. P. Silva, *IEEE Trans. Electron Devices*, 2013, **60**, 2444.

51 M. Socol, N. Preda, C. Breazu, A. Costas, G. Petre, A. Stanculescu, G. Popescu-Pelin, A. Mihailescu and G. Socol, *Nanomaterials*, 2020, **10**, 2366.

52 D. Simatos, L. J. Spalek, U. Kraft, M. Nikolka, X. Jiao, C. R. McNeill, D. Venkateshvaran and H. Sirringhaus, *APL Mater.*, 2021, **9**, 041113.

53 K. Ling, K. Li, W. Zhang and X. Liu, *Adv. Opt. Mater.*, 2023, **11**, 2202456.

54 M. Li, C. An, T. Marszalek, X. Guo, Y. Z. Long, H. Yin, C. Gu, M. Baumgarten, W. Pisula and K. Müllen, *Chem. Mater.*, 2015, **27**, 2218.

55 H. Han, C. Lee, H. Kim and Y. Kim, *Adv. Funct. Mater.*, 2018, **28**, 1800704.

56 Y. Peng, F. Huang, J. Zhang, X. Luo, K. Xu, W. Lv, S. Xu, Y. Wang, Y. Tang, Y. Wei, Z. Xu, Y. Yang and F. Lu, *Org. Electron.*, 2017, **43**, 27.

57 Y. He, J. T. E. Quinn, D. Hou, J. H. L. Ngai and Y. Li, *J. Mater. Chem. C*, 2017, **5**, 12163.

58 J. Kim, D. Khim, J. S. Yeo, M. Kang, K. J. Baeg and D. Y. Kim, *Adv. Opt. Mater.*, 2017, **5**, 1700655.

59 S. Nam, J. Seo, H. Han, H. Kim, D. D. C. Bradley and Y. Kim, *ACS Appl. Mater. Inter.*, 2017, **9**, 14983.

60 Q. Wang, M. Zhu, D. Wu, G. Zhang, X. Wang, H. Lu, X. Wang and L. Qiu, *J. Mater. Chem. C*, 2015, **3**, 10734.

61 F. Huang, Y. Li, H. Xia, J. Zhang, K. Xu, Y. Peng and G. Liu, *Carbon*, 2017, **118**, 666.

62 G. Wang, K. Huang, Z. Liu, Y. Du, X. Wang, H. Lu, G. Zhang and L. Qiu, *ACS Appl. Mater. Inter.*, 2018, **10**, 36177.

63 T. Kim, C. Lee and Y. Kim, *Micromachines*, 2020, **11**, 1.

64 Q. Li, Y. Ran, W. Shi, M. Qin, Y. Sun, J. Kuang, H. Wang, H. Chen, Y. Guo and Y. Liu, *Appl. Mater. Today*, 2021, **22**, 100899.

65 H. Xu, J. Li, B. H. K. Leung, C. C. Y. Poon, B. S. Ong, Y. Zhang and N. Zhao, *Nanoscale*, 2013, **5**, 11850.

66 X. Wang, Y. Zhu, G. Wang and L. Qiu, *Synthetic Met*, 2020, **269**, 116563.

67 H. Han, S. Nam, J. Seo, J. Jeong, H. Kim, D. D. C. Bradley, Y. Kim and I. E. E. E. J. Sel, *Top. Quant.*, 2016, **22**, 6000107.

68 N. Li, Y. Lei, Y. Miao and F. Zhu, *iscience*, 2022, **25**, 103711.

69 C. Lee, J. Kim, Y. Moon, D. Kim, D. Song, H. Kim and Y. Kim, *Asian J. Org. Chem.*, 2018, **7**, 2330.

70 J. Labram, P. Wobkenberg, D. Bradley and T. Anthopoulos, *Org. Electron.*, 2010, **11**, 1250–1254.

71 W. Li, F. Guo, H. Ling, P. Zhang, M. Yi, L. Wang, D. Wu, L. Xie and W. Huang, *Adv. Sci.*, 2017, **4**, 1700007.

72 Y. Guo, J. Zhang, G. Yu, J. Zheng, L. Zhang, Y. Zhao, Y. Wen and Y. Liu, *Org. Electron.*, 2012, **13**, 1969.

73 Z. Shen, Z. Yang, Y. Zhou, Y. Ye, B. Ye, Q. Huang, W. Wu, H. Hong, Z. Hong, Z. Meng, Z. Zeng, S. Ye, Z. Cheng, Q. Lan, J. Wang, Y. Chen, H. Zhang, T. Guo, Y. Ye, Z. Weng and Y. Chen, *J. Mater. Chem. C*, 2023, **11**, 3213.

74 Y. Wang, L. Yin, W. Huang, Y. Li, S. Huang, Y. Zhu, D. Yang and X. Pi, *Adv. Intell. Syst. ger.*, 2021, **3**, 2000099.

75 M. Li, Q. Shu, X. Qing, J. Wu, Q. Xiao, K. Jia, X. Wang and D. Wang, *J. Mater. Chem. C*, 2023, **11**, 5208.

76 T. Miao, W. Liu, C. Huang, B. Cui, R. Chu, X. Zhao, X. Wu, S. Wu, J. Xie, H. Liu, J. Chen, B. Cheng and J. Hu, *J. Mater. Chem. C*, 2023, **11**, 7732.

77 J. Yoon, B. You, Y. Kim, J. Bak, M. Yang, J. Park, M. G. Hahm and M. Lee, *ACS Appl. Mater. Inter.*, 2023, **15**, 18463.

78 S. Kim, J. Yoon, H. Kim and S. Choi, *ACS Appl. Mater. Interfaces*, 2015, **7**, 25479.

79 S. Kim, B. Choi, M. Lim, J. Yoon, J. Lee, H. Kim and S. Choi, *ACS Nano*, 2017, **11**, 2814.

80 S. Kim, M. Lim, Y. Kim, H. Kim and S. Choi, *Sci. Rep.*, 2018, **8**, 2638.

81 T. Xiao, J. Wang, S. Yang, Y. Zhu, D. Li, Z. Wang, S. Feng, L. Bu, X. Zhan and G. Lu, *J. Mater. Chem. A*, 2020, **8**, 401.

82 X. Feng, Y. Wang, T. Xiao, Z. Shen, Y. Ren, G. Lu and L. Bu, *Front. Chem.*, 2020, **8**, 211.

83 Y. Peng, F. Huang, J. Zhang, X. Luo, K. Xu, W. Lv, S. Xu, Y. Wang, Y. Tang, Y. Wei, Z. Xu, Y. Yang and F. Lu, *Org. Electron.*, 2017, **43**, 27.

84 S. Lan, J. Zhong, E. Li, Y. Yan, X. Wu, Q. Chen, W. Lin, H. Chen and T. Guo, *ACS Appl. Mater. Inter.*, 2020, **12**, 31716.

85 Y. Ke, R. Yu, S. Lan, L. He, Y. Yan, H. Yang, L. Shan, H. Chen and T. Guo, *J. Mater. Chem. C*, 2021, **9**, 4854.

86 S. Lan, J. Zhong, J. Chen, W. He, L. He, R. Yu, G. Chen and H. Chen, *J. Mater. Chem. C*, 2021, **9**, 3412.